Elastohydrodynamics of swimming helices: Effects of flexibility and confinement

John LaGrone,* Ricardo Cortez,† and Lisa Fauci‡
Department of Mathematics, Tulane University, New Orleans, Louisiana 70118, USA

(Received 16 November 2018; published 25 March 2019)

Motivated by bacterial transport through porous media, here we study the swimming of an actuated, flexible helical filament in both three-dimensional free space and within a cylindrical tube whose diameter is much smaller than the length of the helix. The filament, at rest, has a native helical shape modeled after the geometry of a typical bacterial flagellar bundle. The finite length filament is a free swimmer and is driven by an applied torque as well as a countertorque (of equal strength and opposite direction) that represents a virtual cell body. We use a regularized Stokeslet framework to examine the shape changes of the flexible filament in response to the actuation as well as the swimming performance as a function of the nondimensional *Sperm number* that characterizes the elastohydrodynamic system. We also show that a modified Sperm number may be defined to characterize the swimming progression within a tube. Finally, we demonstrate that a helical filament whose axis is not aligned with the tube axis can exhibit centering behavior in the narrowest tubes.

DOI: 10.1103/PhysRevFluids.4.033102

I. INTRODUCTION

At the microscale, bacterial motility is achieved through the action of rotating helices [1]. Monotrichous cells such as *Pseudomonas aeruginosa* are propelled by a single helical flagellum driven by a rotary motor at its base. Peritrichous cells such as *Escherichia coli* are propelled by many helical flagella that, when rotating in the same direction, form a coherent helical bundle. A fascinating family of bacteria, spirochetes, have cell bodies that are themselves helical and appear to move as a corkscrew through viscous fluids [2]. In addition to nature's swimming helices, fabricated helical micromachines present intriguing possibilities in biomedical applications such as drug delivery [3,4]. While varying in their material properties, these helices (individual bacterial flagella, flagellar bundles, spirochete cells, fabricated helices) are elastic structures that, when actuated in a viscous fluid, could experience shape deformation in response to the flow.

It is also of interest, both for engineered helical microswimmers and natural bacterial cells, to understand how motility is affected when moving through confined environments. Indeed, the use of bacteria in bioremediation often relies on cells moving through porous media such as soil, where the pore sizes are smaller than the flagellar length [5]. The effects of moving through such restrictive geometries on the swimming performance of bacterial cells have been examined in both laboratory experiments and mathematical models. Early experiments [6] of *E. coli* swimming in glass capillary tubes of 3 μm diameter showed that the cells could not tumble and reorient in this confined space and exhibited unidirectional motion. More recently, it was shown that such tumbling of *E. coli* was also hindered when cells were swimming close to a planar surface. Microfluidic experiments

*jlagrone@tulane.edu
†rcortez@tulane.edu
‡fauci@tulane.edu

showed that *E. coli* cells tend to swim in helical paths in narrow capillaries [5] and *S. marcescens* experienced a sizable boost in swimming velocity in microchannels [7].

Models of microbial swimming in cylindrical capillary tubes study the performance of spherical squirmers [8] and dipolar swimmers [9]. Using a boundary element method, Zhu *et al.* [8] show that spherical squirmers with tangential deformations swim more slowly as confinement increases, but swimmers with normal deformations swim more quickly with confinement. The reduced model swimmers in Ref. [9] moving in the center of a rigid tube move faster with confinement. Two models of a swimmer in a capillary tube that represent the detailed geometry of a rotating rigid helix were presented by Liu *et al.* [10] and Li and Spagnolie [11]. In these models, both the tube and the helix were infinitely long, but the radius of the tube was on the order of the helical radius. Except for the tightest confinements, swimming speed increased with confinement when a fixed torque was applied. A recent model of a finite helical swimmer propelling an ellipsoidal cell body in a cylindrical tube uses the commercial software COMSOL to study its speed and efficiency when the helix rotational speed and geometry are prescribed [12]. It was found that for thick flagellated swimmers, there was an optimal radius of the tube that maximized speed and efficiency depending upon the geometric parameters of the helix.

As in the model of Ref. [10], here we study the swimming of an actuated helical filament in a capillary tube whose radius is close to the helix radius. However, the helical filament in this study is flexible and of finite length. Using a regularized Stokeslet framework [13], we first examine the swimmer in free space and show that its performance is well characterized by the Sperm number, a nondimensional parameter that measures the ratio of viscous fluid forces to elastic forces. We then examine the effects of confinement in a tube and suggest a modification of the Sperm number to account for the effect of the tube surface. Finally, because the helical filament is of finite length, we can study its dynamics when it is initialized at an angle to the centerline of the tube.

II. METHODOLOGY

A. Stokes equations

We model a flexible, helical filament that is actuated by applied torques in a viscous fluid, where the length and timescales are small enough that inertial forces are negligible. The fluid motion is therefore well modeled by the incompressible Stokes equations:

$$0 = -\nabla \hat{P} + \mu \Delta \hat{\mathbf{u}} + \hat{\mathbf{F}} + \tfrac{1}{2}\nabla \times \hat{\mathbf{L}}, \quad 0 = \nabla \cdot \hat{\mathbf{u}}, \tag{1}$$

where $\hat{P}$ is the pressure, $\hat{\mathbf{u}}$ is the fluid velocity, μ is the fluid viscosity, $\hat{\mathbf{F}}$ is the force per volume exerted by the elastic helical filament, and $\hat{\mathbf{L}}$ is the torque per volume applied to rotate the filament and the virtual cell body in the opposite direction.

The forces and torques in Eq. (1) will be localized at the helical filament. These equations hold in all of three-dimensional space. To nondimensionalize the problem, we assume characteristic scales for length $\hat{\ell}$, time $\hat{T}$, force $\hat{\mathcal{F}}$, and torque $\hat{\mathcal{L}}$. By choosing $\mathcal{F} = \mu\hat{\ell}^2/\hat{T}$ and $\mathcal{L} = \mu\hat{\ell}^3/\hat{T}$, the dimensionless Stokes equations are

$$0 = -\nabla p + \Delta \mathbf{u} + \mathbf{F} + \tfrac{1}{2}\nabla \times \mathbf{L}.$$

Throughout this paper, we choose the characteristic scales to be $\hat{\ell} = 4\,\mu$m, $\hat{T} = 0.01$ s, μ to be the viscosity of water, and, hence, $\mathcal{F} = 1.6 \times 10^{-12}$ N.

We use a regularized Stokeslet framework [13] to model the elastohydrodynamic system, where the external force comes from a surface integral of regularized forces supported on the cylindrical surface of the helical filament, while the regularized torques are applied only at two points $\mathbf{y}_1$ and $\mathbf{y}_2$. The first torque will be applied at the tip of the helix, whereas the second, of equal strength but opposite direction, will be applied slightly in front of the filament, as a proxy to a counter-rotating

cell body. The expressions for force and torque are

$$\mathbf{F}(\mathbf{x}) = \int_{\Sigma} \mathbf{f}(\mathbf{y})\phi_{\epsilon}(\mathbf{x}-\mathbf{y})dS_y, \quad \mathbf{L}(\mathbf{x}) = \sum_{k=1}^{2} \mathbf{g}_k \phi_{\epsilon}(\mathbf{x}-\mathbf{y}_k).$$

The regularization (or blob) function is chosen to be

$$\phi_{\varepsilon}(\mathbf{x}-\mathbf{y}) = \frac{15\varepsilon^4}{8\pi(r^2+\varepsilon^2)^{7/2}}, \tag{2}$$

where $r = \|\mathbf{x}-\mathbf{y}\|$. This leads to the velocities due to the regularized Stokeslets and rotlets as follows:

$$\mathbf{u}_{st}(\mathbf{x}) = \int_{\Sigma} S_{\varepsilon}(\mathbf{x},\mathbf{y})\mathbf{f}(\mathbf{y})dS_y = \frac{1}{8\pi}\int_{\Sigma} \frac{(r^2+2\varepsilon^2)\mathbf{f}(\mathbf{y}) + [\mathbf{f}(\mathbf{y})\cdot(\mathbf{x}-\mathbf{y})](\mathbf{x}-\mathbf{y})}{(r^2+\varepsilon^2)^{3/2}} dS_y. \tag{3}$$

$$\mathbf{u}_{rt}(\mathbf{x}) = \sum_{k=1}^{2} R_{\varepsilon}(\mathbf{x},\mathbf{y}_k)\mathbf{g}_k = \frac{1}{16\pi}\sum_{k=1}^{2} \frac{2r_k^2+5\varepsilon^2}{\left(r_k^2+\varepsilon^2\right)^{5/2}}(\mathbf{g}_k \times (\mathbf{x}-\mathbf{y}_k)), \tag{4}$$

where $\mathbf{f}(\mathbf{y})$ is force per unit area, Σ denotes the surface of the helical filament, $\mathbf{g}_k$ is torque, $r = |\mathbf{x}-\mathbf{y}|$, $r_k = |\mathbf{x}-\mathbf{y}_k|$, and ε is the regularization parameter. We note that these velocities are defined everywhere in $\mathbb{R}^3$ and are everywhere incompressible.

B. Representation of helical filament and its actuation

The model elastic filament that we consider has a native helical equilibrium shape whose centerline is given by

$$\begin{aligned} x(s) &= \alpha(s), \\ y(s) &= -r_h(s)\cos\left(\frac{(2\pi n_p)s}{L}\right), \quad 0 \leqslant s \leqslant L, \\ z(s) &= r_h(s)\sin\left(\frac{(2\pi n_p)s}{L}\right), \end{aligned} \tag{5}$$

where L is the arc length of the helix, n_p is the number of turns in the helix, and the helical radius, tapered from back to front, is given by

$$r_h(s) = A\left[\frac{1}{\pi}\arctan\left(\frac{\beta s}{L}-1\right)+\frac{1}{2}\right]. \tag{6}$$

As in Ref. [14], $\alpha(s)$ is chosen such that the tangent vector $[x'(s), y'(s), z'(s)]$ has unit length, so that s is an arclength parameter. We do not view the helical filament as a single bacterial flagellum but rather as a representation of a bacterial flagellar bundle. In this work, we choose a fixed equilibrium configuration of the helical filament in all simulations, whose associated geometric parameters are given in Table I. These fall within the range of parameters for a typical, loosely packed helical bundle [1,15,16].

We construct the discretization of the surface of the cylindrical helical filament by placing hexagonal cross sections of radius R_f along the helical centerline, perpendicular to the centerline. As such, each cross section is discretized by $N_c = 6$ six points, and we take N_f cross sections along the helical filament so that the spacing between neighboring cross sections is approximately equal to the spacing between adjacent points on a cross section (see Fig. 1). Each of the $N = N_c \times N_f$ discrete points on the surface of the filament is connected to a subset of the other surface points by a Hookean spring, giving elasticity to the structure. We define the dimensionless elastic energy in

TABLE I. Input parameters, computed quantities, and numerical parameters used in computations.

Input quantities	Dimensionless value	Corresponding dimensional value
Helix arc length, L	5.42	21.7 μm
Helix projected length, l	3.93	15.7 μm
Number of pitches, n_p	2	2
Helix max amplitude, A	0.5	2 μm
Tapering parameter, β	6	6
Filament radius, R_f	0.08	0.32 μm
Rotlet strength σ (=0.5 torque)	1.0–7.0	(6.4–44.8) $\times 10^{-18}$ N-m
Spring stiffness, k	75–1200	1.2×10^{-10} to 1.92×10^{-9} N
EI	2.36–37.1	(6.0–96.5) $\times 10^{-23}$ N-m^2
Counter rotlet separation, τ	.50	2 μm
Computed quantities		
Frequency, ω	0.024–0.67	2.4–67 Hz
Swimming speed, U	0.0057–0.14	2.28–55.5 μm/s
Distance per revolution	0.05–0.34	0.20–1.4 μm
Numerical parameters		
Cross sections along helix, N_f	65	65
Points per helical cross section, N_c	6	6
Cross sections along tube, N_t	64	64
Points per tube cross section, N_θ	24–38	24–38
Spacing between helix nodes, Δs_h	0.08	0.32 μm
Helix blob size, ϵ_h	0.025	0.1 μm
Spacing between tube nodes, Δs_t	0.16	0.64 μm
Tube blob size ϵ_t	0.05	0.2 μm
Time step, Δt	2.5×10^{-6}–1.0×10^{-5}	2.5×10^{-8}s–1.0×10^{-7}s

the system as

$$\mathcal{E} = \frac{1}{2} \sum_j k_j l_j \left(\frac{\left\| \mathbf{x}_{j_1} - \mathbf{x}_{j_2} \right\|}{l_j} - 1 \right)^2, \tag{7}$$

where k_j is the stiffness of a spring with resting length l_j that connects points j_1 and j_2. The sum is over all springs. The force at $\mathbf{x}_{j_1}$ is $\mathbf{f}_{j_1} A_{j_1}$, where A_{j_1} is the area of a patch of surface centered at $\mathbf{x}_{j_1}$

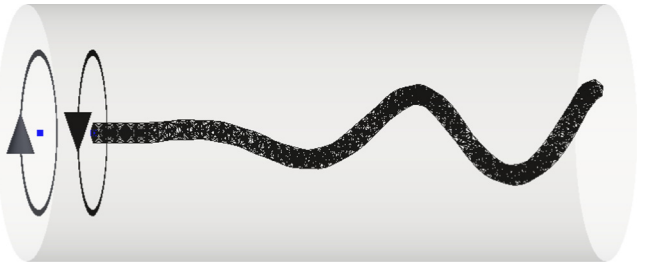

FIG. 1. Computational helical filament consisting of a network of springs. The figure shows the equilibrium configuration. The motion is generated by the activation of a torque at the center of the front cross section and by the countertorque, which is placed a small distance in front of the first cross section where the cell body might be.

in the discretization. We have that

$$\mathbf{f}_{j_1} A_{j_1} = -\frac{\partial \mathcal{E}}{\partial \mathbf{x}_{j_1}}.$$

Similar constructs of semiflexible filaments using nodes with elastic linkages have been used to model diatom chains [17] and bacterial flagella [14,18]. In all simulations shown here, we choose a spring topology so that each point on a given cross section is connected to every other point on that cross section, as well as to every other point on the two cross sections adjacent to it. This means that each node is connected to $5 + 2 \times 6 = 17$ other nodes. In addition, in all simulations shown, the stiffness constant $k_j = k$ in Eq. (7) is taken to be the same for all springs. The resting lengths of the springs, l_j, in Eq. (7) do vary with j and are computed during the construction of the helical surface. The initialized helical filament configuration is in its equilibrium state [the total energy in Eq. (7) is zero].

As in bacterial flagella that are driven by a rotary motor at their base, we actuate the helical filament by a regularized torque that is placed at the centroid of the first cross section $\mathbf{y}_1$. We apply a countertorque of the same strength and opposite direction in front of the first cross section, at a fixed distance away. In practice, this is done by computing the outward normal to the first cross section $\mathbf{n}$ and choosing $\mathbf{y}_2 = \mathbf{y}_1 + \tau \mathbf{n}$, where τ is a positive parameter. Because of these applied torques, the flexible filament will depart from its equilibrium shape as the network springs become stretched or compressed, causing forces at the nodes to develop. The fluid velocity due to these elastic forces and the applied torques is evaluated at each material point $\mathbf{x}_i$, $i = 1, ..., N$ of the helical surface, using Eq. (4) and a discrete version of Eq. (3):

$$\mathbf{u}(\mathbf{x}_i) = \sum_{k=1}^{2} R_\varepsilon(\mathbf{x}_i, \mathbf{y}_k)\mathbf{g}_k + \sum_{j=1}^{N} S_\varepsilon(\mathbf{x}_i, \mathbf{x}_j)\mathbf{f}_j A_j.$$

For a swimmer in free space, this velocity is used to update the positions of the nodes of the flexible filament, satisfying the no-slip boundary condition of Stokes flow. Note that since all forces arise from springs and the torque driving the filament is balanced by a countertorque representing the cell body, the sum of forces and torques are zero, and hence momentum and angular momentum are conserved. The actuated flexible helix is a free swimmer.

C. Coupled helix-tube system

We wish to examine the swimming of the actuated helical filament described above in a rigid, cylindrical tube whose radius R is smaller than the filament length but whose length is long enough so that no end effects on the fluid dynamics are present. The surface of the tube is discretized by N_t circular cross sections with N_θ points each, for a total of $N_{\text{tube}} = N_t \times N_\theta$ points. Regularized forces on these N_{tube} points $\mathbf{z}_i$ will be computed so that the no-slip (zero velocity) condition is satisfied. These forces, plus the elastic forces supported on the helical filament and the applied torques, will determine the fluid velocity at any point in the tube, along with the filament's swimming progression. Here we describe the overall algorithm for evolving this coupled helix-tube system:

Given helix surface points and forces $\mathbf{x}_j, \mathbf{f}_j$, $j = 1, ..., N$ and torques $\mathbf{g}_1, \mathbf{g}_2$:

(1) Compute the velocities on the N_{tube} tube surface points that are induced by these forces and torques:

$$\tilde{\mathbf{u}}(\mathbf{z}_i) = \sum_{k=1}^{2} R_\varepsilon(\mathbf{z}_i, \mathbf{y}_k)\mathbf{g}_k + \sum_{j=1}^{N} S_\varepsilon(\mathbf{z}_i, \mathbf{x}_j)\mathbf{f}_j A_j.$$

(2) Compute forces $\mathbf{h}_i$ that must be exerted on the tube points so that the velocity $\tilde{\mathbf{u}}$ is canceled out there:

$$-\tilde{\mathbf{u}}(\mathbf{z}_i) = \sum_{j=1}^{N_{\text{tube}}} S_\varepsilon(\mathbf{z}_i, \mathbf{z}_j)\mathbf{h}_j \hat{A}_j.$$

This is a $3N_{\text{tube}} \times 3N_{\text{tube}}$ linear system for the unknown forces $\mathbf{h}_j$. We note that the (dense) coefficient matrix depends upon the relative distances between the discrete nodes on the tube's surface which do not change in time. This allows us to precompute its factorization once, even though the system is solved at every time step.

(3) Finally, exploiting linearity of the Stokes equations, the velocities of the material points on the helical filament are

$$\mathbf{u}(\mathbf{x}_i) = \sum_{k=1}^{2} R_\varepsilon(\mathbf{x}_i, \mathbf{y}_k)\mathbf{g}_k + \sum_{j=1}^{N} S_\varepsilon(\mathbf{x}_i, \mathbf{x}_j)\mathbf{f}_j A_j + \sum_{j=1}^{N_{\text{tube}}} S_\varepsilon(\mathbf{x}_i, \mathbf{z}_j)\mathbf{h}_j \hat{A}_j.$$

A forward Euler method is used to evolve the positions of the helix. We note that more rigid helices require smaller time steps than flexible ones in this explicit time-stepping procedure. The positions of the two applied torques are also evolved relative to the helix. The numerical parameters used are shown in Table I.

We remark that we also modify this algorithm to study the swimming of a *rigid* helix within a tube, driven by the torque-coutertorque actuation described above. In this case, given the applied torques, we need to solve for a distribution of forces at the discrete points of the tube surface and those of the helix surface so that (a) the fluid velocity is zero at the tube nodes and (b) the velocity at the helix nodes is that of a rigid translation $\mathbf{U}$ and rotation $\boldsymbol{\Omega}$. The six unknowns $\mathbf{U}$, $\boldsymbol{\Omega}$ are determined by enforcing the conditions of free swimming (total forces and torques are zero on swimmer). We note that this entails solving a large linear system of size $3(N_{\text{tube}} + N + 2) \times 3(N_{\text{tube}} + N + 2)$.

D. Sperm number

As in other elastohydrodynamic systems where flexible fibers are coupled to a viscous, incompressible fluid, the relative importance of flow forces to elastic forces is an important nondimensional parameter that governs system performance (e.g., Refs. [19–21]). Following Ref. [19], we define the Sperm number:

$$\text{Sp}^4 = \frac{\xi^\perp \omega L^4}{EI}, \tag{8}$$

where

$$\xi^\perp = \frac{4\pi}{\log\left(\frac{L}{R_f}\right) + 1}. \tag{9}$$

Here, L is the arc length of the helical filament, R_f is its cross-sectional radius, EI is its bending rigidity, and ω is the rotational frequency achieved for the input torques. The perpendicular drag on the filament in free space is approximated by $\xi^\perp$ in Eq. (9).

Within this setup, the macroscopic bending rigidity EI of the node-spring structure depends upon the individual spring constants k_j and the topology of the spring network. As first described in Ref. [18] and used in Ref. [17], we can precompute the EI for the node-spring structure as follows: We construct a straight cylindrical fiber with the same node-spring topology and same individual spring constants, and then bend it into a circular arc with a prescribed radius of curvature κ. We then compute the resulting energy in the node-spring system using Eq. (7), arriving at

$$EI = \frac{2\mathcal{E}}{\kappa^2 L}. \tag{10}$$

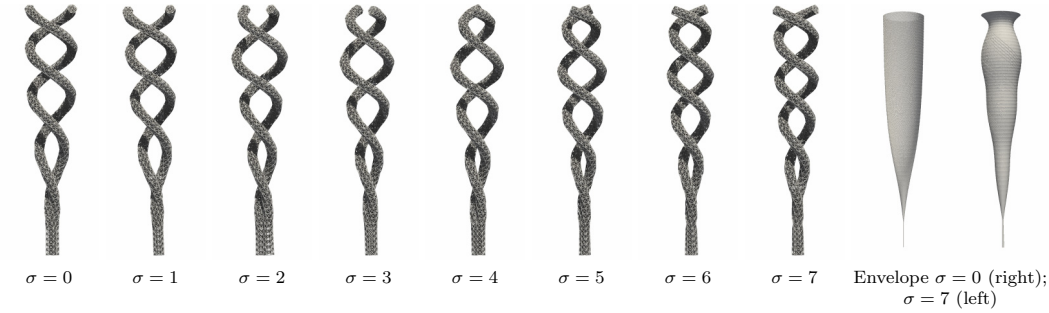

FIG. 2. Achieved shapes of the helical filament for a fixed stiffness constant $k = 300$ and varying torque magnitudes (from left to right, first eight panels). Each of these panels shows the filament at two different phases for visualization purposes. The leftmost image corresponds to the equilibrium configuration without the dynamics ($\sigma = 0$). Subsequence images correspond to increasing the regularized rotlet magnitude by one dimensionless unit. The rightmost two panels show the envelope formed by the centerline of the filament as it rotates through one revolution for both the equilibrium (rigid) configuration and for the flexible case with $\sigma = 7$.

While the flexible helical filaments, we study are motivated by bacterial flagellar bundles, we remark that the range of bending rigidities that we examine here are at the low range of bending rigidities of single bacterial flagella ($EI \approx 10^{-24}$–10^{-21} N m^2) [3,22].

III. RESULTS AND DISCUSSION

A. Flexible swimmer in free space

We first consider the dynamics of the actuated model helical filament in free space. In all of the simulations presented in this paper, the equilibrium helical shape is fixed, as is the placement of the torque-countertorque actuation (Table I). We will, however, vary two input parameters: the stiffness of the springs comprising the filament k and the strength of the rotlet σ that drive the rotation. We choose first to vary these separately and then analyze results in terms of the nondimensional Sperm number.

Figure 2 shows snapshots of the emergent shapes of the same helical filament with stiffness constant $k = 300$ actuated with increasing rotlet strengths (from left to right, first eight panels). These snapshots are taken at times after the elastic structure has settled into a steady shape. For each rotlet strength $\sigma = 0, 1, ..., 7$, two projected images of the helix are shown. Note that the case of rotlet strength, zero is the equilibrium configuration of the helix. Of course, if the helix were rigid ($k = \infty$), it would maintain its equilibrium shape for each rotlet strength. However, for this flexible filament ($k = 300$), we see that stronger actuation gives rise to smaller amplitude and larger wave numbers (more turns in the helix). Such changes in pitch and helical radius for rotating flexible helices were also noted in the resistive force theory calculations of Takano *et al.* [23].

The case $\sigma = 0$ indicates no rotation, and hence no deviation from equilibrium shape, which is analagous to the shape that would be realized in the rotation of a rigid helical filament. The rightmost two panels of Fig. 2 show the envelope formed by the centerline of the filament as it rotates through one revolution for the equilibrium (rigid) configuration ($\sigma = 0$) and the flexible helix with $\sigma = 7$. Although the envelope of the rigid rotation shows that the helix radius increases monotonically from base to tip as specified, the envelope in the flexible case shows a shape deformation with multiple local maxima of helical radius. These results are reminiscent of the experiments in Ref. [24] where a flexible, natively straight filament was rotated in a viscous fluid. Here, a wrapping transition to helicity was demonstrated, with smaller amplitude and larger wave numbers emerging for larger rotation speeds.

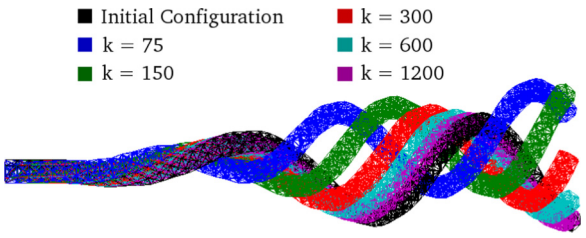

FIG. 3. Achieved shapes of the helical flagellum for a fixed rotlet magnitude of 5 dimensionless units and varying spring stiffness constants. All images are shown at the same time of simulation.

Figure 3 shows snapshots of five helical filaments with different stiffnesses actuated by the same rotlet strength $\sigma = 5$, along with the equilibrium configuration ($k = \infty$, in black). As in Fig. 2, swimming progression is not shown because the images are repositioned so that their front sections coincide. This qualitative comparison of emerging shapes demonstrates that the more flexible filaments actuated at the same strength exhibit larger wave numbers.

Figures 4(a) and 4(b) show the swimming speed and the rotational frequency for each helical filament as a function of rotlet strength. For the rigid filament, both speed and rotational frequency increase linearly with rotlet strength, as expected. For a fixed rotlet strength, however, we see that swimming speed decreases with flexibility while rotational frequency increases, i.e., for the same input torque, flexible helices spin faster but swim more slowly. Figure 4(c) shows the distance

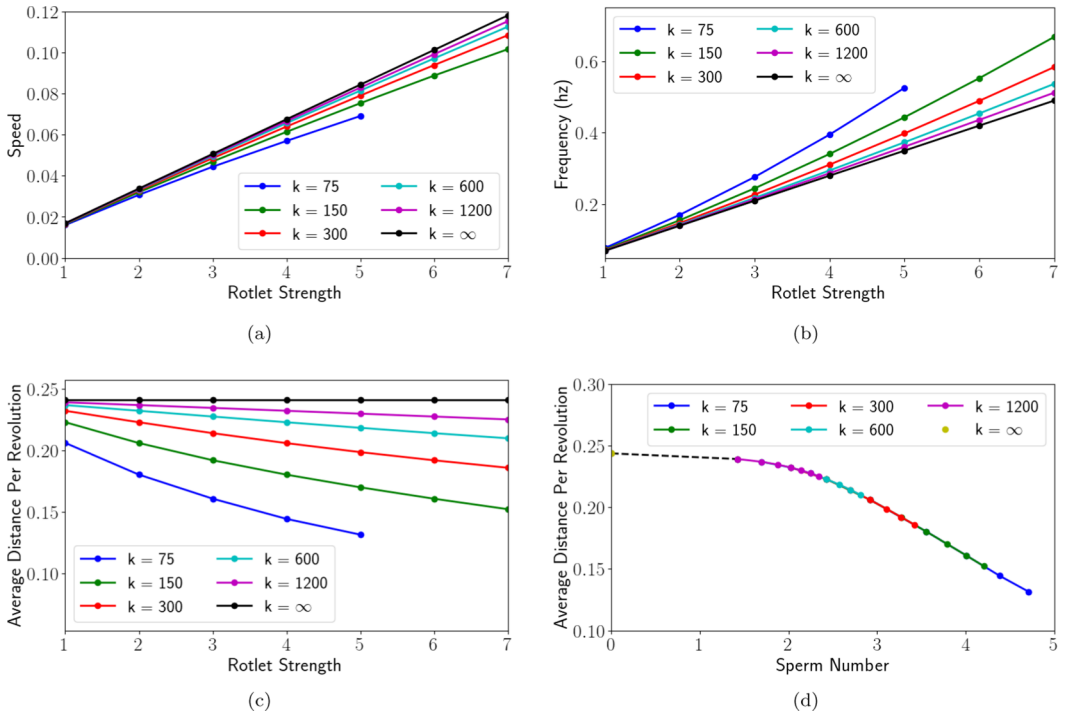

FIG. 4. (a)–(c) Swimming speed, rotational frequency, and average swimming distance per revolution as a function of regularized rotlet magnitude. The different curves correspond to different spring stiffness constants. (d) The same data as in (c) plotted as a function of sperm number. Different colors correspond to different spring stiffness constants and the data points of a given color correspond to different rotlet magnitudes.

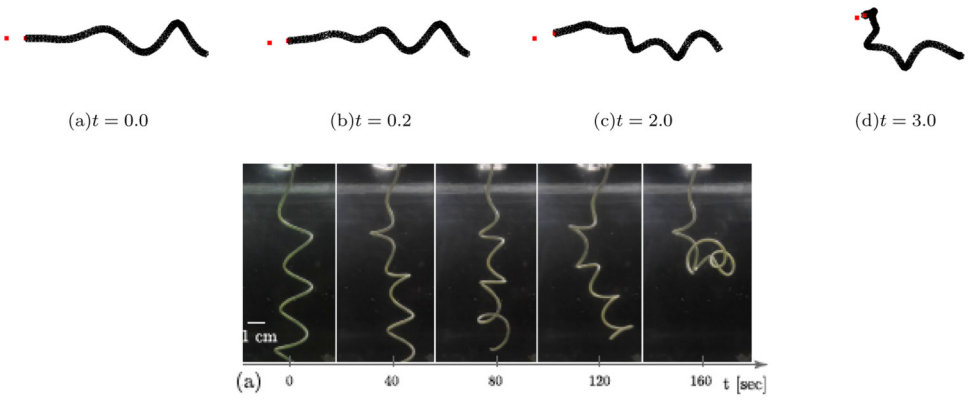

FIG. 5. [(a)–(d)] Snapshots from a simulation with applied rotlet strength of 7 dimensionless units and relatively low stiffness constant $k = 75$. (e) Buckling observed experimentally (Reprinted figure with permission from M. K. Jawed *et al.*, Phys. Rev. Lett. **115**, 168101 (2015). Copyright (2015) by the American Physical Society).

per revolution (translational distance per one spin of the helix) as a function of rotlet strength. For the rigid helical filament, this is constant. As flexibility increases, the distance per revolution decreases. Although the helical filament is not perfectly inextensible, because of the many cross linkages between nodes the variation of its total arc length during the course of a simulation is very small. Even for the simulations of the most flexible helices ($k = 75$) described in Figs. 4(a) and 4(b), the arc length varies by less than 1% from the equilibrium arc length.

While the stiffness of the helical filament and the strength of the applied torque are two things that can be controlled separately in laboratory experiments (and in computational experiments), we see that increasing applied torque for a filament of a given stiffness is akin to decreasing filament stiffness for a given applied torque. Of course, this is evident in the definition of the Sperm number Sp [Eq. (8)], which is a multiple of the ratio of rotational frequency to filament bending rigidity. We remark that while we do input torque, the rotational frequency is an output of the coupled fluid-filament system, so we do not know Sp *a priori*. Figure 4(d) shows the distance per revolution measured for each of the computational simulations (six filaments of different stiffness actuated at seven rotlet strengths) plotted as a function of the nondimensional Sperm number. The data in Fig. 4(c) collapse nicely onto one curve. For the smallest Sperm numbers, the distance per revolution is nearly constant, but then decreases linearly for $\mathrm{Sp} > 2.5$.

Note that in Figs. 4(a)–4(c) no swimming data are reported for the most flexible filament ($k = 75$) actuated at the largest rotlet strengths of $\sigma = 6, 7$. While all of the filaments in the other simulations relaxed into a steady shape, resulting in periodic swimming motion, the most flexible filament that was actuated too quickly exhibited the buckling behavior shown in Figs. 5(a)–5(d). These snapshots show the time evolution of body shape, with the last frame Fig. 5(d) demonstrating the total loss of a straight, helical axis.

Figure 5(e) shows results of recent laboratory experiments of a rotating flexible helix in a viscous fluid, exhibiting this type of buckling [25]. This work quantified the dynamics of the underlying mechanical instability and used both experiments and slender-body theory calculations to determine a critical rotational velocity ω_b for a given helix at which buckling would occur. For each applied rotation ω, a resulting propulsive force $\hat{F}_p$, nondimensionalized as $F_p = \hat{F}_p L^2/EI$ was measured. Up until the critical rotational velocity ω_b, F_p would increase as a function of ω, but then the propulsive force would drop dramatically as the helix buckled. While the experiments using a tethered helix measure the dropoff in propulsive force to monitor buckling, our free-swimmer calculations show the analogous dropoff in forward swimming progression when buckling occurs. Computational

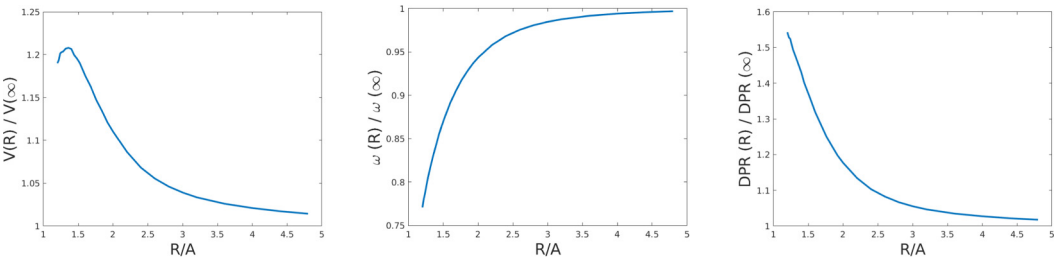

(a) (b) (c)

FIG. 6. Swimming speed, rotational frequency, and swimming distance per revolution computed as a function of tube radius for the case of a *rigid* helical flagellum whose axis is aligned with the tube axis. The tube radius is scaled by the maximum flagellum amplitude. The computed quantities are scaled by their corresponding value in the absence of tube.

experiments have also demonstrated this buckling, called a "whirling instability," in Refs. [18,26]. We remark that buckling instabilities in *the flagellar hook* have been implicated as a mechanism for reorienting bacterial swimming trajectories [1,27].

B. Flexible swimmer in tube: aligned with tube axis

We next place our model filament inside a straight, cylindrical tube so that the straight axis of the helix coincides with the centerline of the tube (as in Fig. 1). Liu *et al.* [10] considered a related system, where a *rigid, infinitely long* helix was driven, either by fixed torque or fixed rotational velocity, to swim inside a capillary tube. They found that for a fixed applied torque, in all but the narrowest tubes, swimming velocity increased with confinement, until the radius of the tube was about 40% more than that at which the helix would touch the walls of the tube. We first perform a series of simulations for a *rigid, finite* helical filament with the same geometric parameters as in Table I, varying the radius of the tube R. Note that the minimum value of this radius in our simulations would be $R = A + R_f$. Figure 6(a) shows, for a fixed torque, the velocity of the helix in a tube of radius R normalized by its velocity in free space as a function of the scaled tube radius R/A. Here we see the same nonmonotonic behavior in swimming speed as a function of tube radius for the finite helical swimmer as reported in Ref. [10]. Figure 6(b), however, shows that for a fixed applied torque, the rotational frequency of the helical filament decreases monotonically with confinement, dropping off dramatically as the helix almost touches the tube walls. Figure 6(c) shows that the distance per revolution increases monotonically with confinement—for a tightly fitting helix, the translational distance per turn is greatest in the tightest fits but that turn takes a much longer time to complete.

We now examine the swimming dynamics of the *flexible* helical filaments in tubes of varying radii, again initialized with their axis coinciding with tube axis. Figure 7(a) shows the swimming speed of the flexible helical filament with $k = 300$ as a function of rotational frequency ω in tubes of radii $R = 0.7, 0.8, 1.0, 1.2$ as well as in free space $R = \infty$. Note that these simulations were performed by varying the input rotlet strength and the rotational frequency is an output of the calculation. As expected, Fig. 7(a) indicates that for each tube radius, the swimming speed increases with rotational frequency. We also see that the emergent rotational frequency for a fixed torque decreases as the tube diameter decreases. Finally, for all tube radii presented in Fig. 7(a), we see that swimming speed increases with confinement for this flexible helix. Here we have not included simulations in the narrowest tubes, as in Fig. 6(a), which would show a dropoff in speed as radius decreases.

Figure 7(b) shows the distance per revolution achieved by actuated helical filaments in a series of simulations that varied the stiffness of the springs comprising the filament k, the applied rotlet strength σ, and the tube radius R as a function of Sp. Note that the curve for $R = \infty$ corresponds

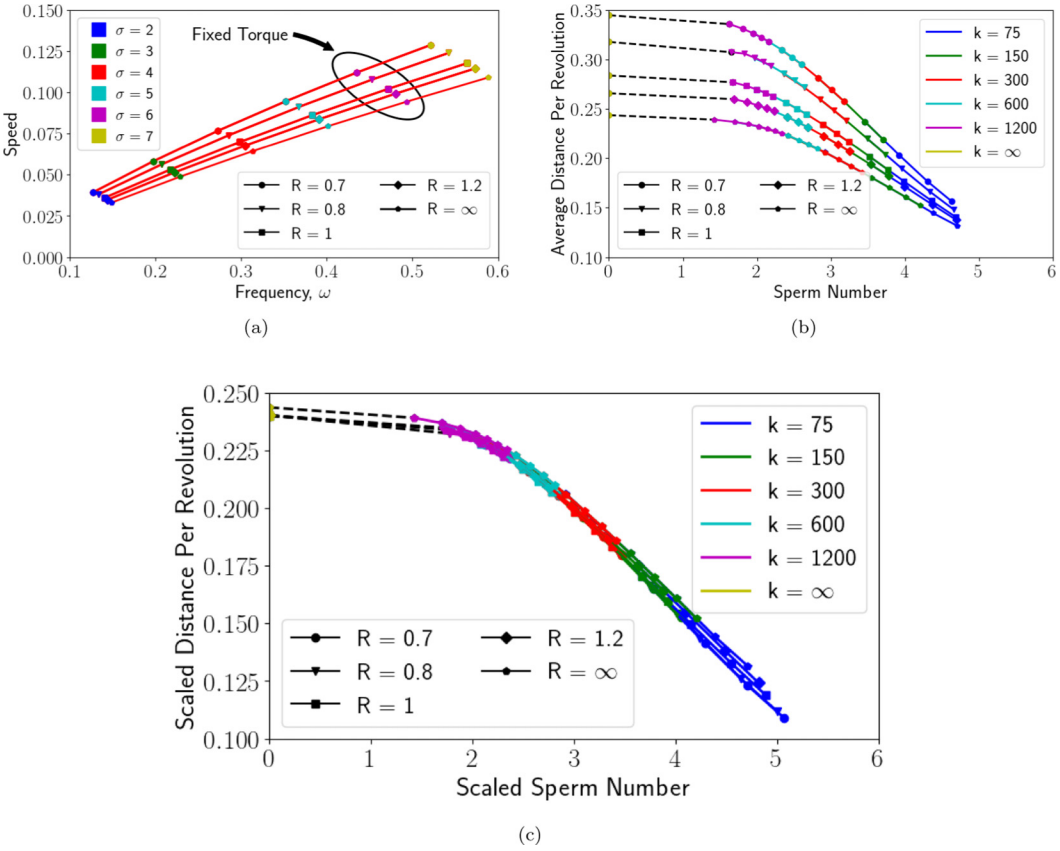

FIG. 7. (a) Swimming speed plotted as a function of frequency for $k = 300$ (other values of k are similar). Each curve corresponds to a different tube radius and the points on each curve were computed by applying different torque magnitudes. (b) Swimming distance per revolution plotted as a function of the Sperm number. The colors indicate the varying spring stiffnesses, k, and each curve corresponds to a different tube radius. The points of a given color along a curve were computed by varying the rotlet strength. (c) Same data as in panel (b) but plotted as a function of the modified Sperm number in a tube given in Eq. (16)

to Fig. 4(d). However, we see that the data collapse to different curves, depending upon the tube radius. We have already seen that the presence of the tube affects its swimming speed and rotational velocity for an applied torque. It also affects the drag force on the helical filament. We estimate this effect by assuming that the tube-helix system is equivalent to a helix swimming in free space with an effective drag coefficient that depends upon the tube radius R. Let $U(R)$ be the swimming velocity of the helix in a tube of radius R and $C_D(R)$ be the drag coefficient. The drag force on the helical filament in the presence of the tube is conceived as the same force resulting from motion in free space (at velocity U^∞) with a modified drag coefficient:

$$F_D = C_D(R)U(R) = [C_D(R)f(R)]U^\infty.$$

Motivated by the work done in Ref. [28] for a sphere, we assume

$$f(R) = 1 + \gamma_1\left(\frac{R_f}{R}\right) + \gamma_2\left(\frac{R_f}{R}\right)^2 + \gamma_3\left(\frac{R_f}{R}\right)^3, \tag{11}$$

so that as $R \to \infty$, we get $F_D = C_D^\infty U^\infty = \xi^\perp U^\infty$.

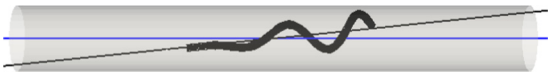

FIG. 8. Initial orientation of a flagellum angled 0.1 rad away from the central axis of a tube. The centerline of the tube is indicated by the blue line and the black line is the centerline of the targeted configuration of the filament.

Note that the drag can also be interpreted as

$$F_D = C_D(R)U(R) = C_D(R)[U^\infty f(R)],$$

which says that the presence of the tube modifies the swimming speed by the same function $f(R)$.

In addition, we assume that the presence of the tube modifies the angular velocity of the helical filament through a modified rotational drag coefficient: $Q_D(R)w(R) = Q_D(R)[w^\infty/g(R)]$ where

$$g(R) = 1 + \alpha_1\left(\frac{R_f}{R}\right) + \alpha_2\left(\frac{R_f}{R}\right)^2 + \alpha_3\left(\frac{R_f}{R}\right)^3. \tag{12}$$

In order to estimate the coefficients in Eqs. (11) and (12), we perform a least squares fit to our velocity and angular velocity data from simulations only in the case of the *rigid* helical filament:

$$\gamma_1 = 0.3371, \quad \gamma_2 = -1.7293, \quad \gamma_3 = 1.2798, \tag{13}$$

and

$$\alpha_1 = -0.0172, \quad \alpha_2 = 0.0092, \quad \alpha_3 = 0.5261. \tag{14}$$

The distance per rotation of the helical filament is

$$\frac{U(R)}{w(R)} = \frac{[f(R)g(R)]U^\infty}{w^\infty}, \tag{15}$$

and we thus define a scaled distance per revolution by dividing by the values plotted in Fig. 7(b) by $f(R)g(R)$.

Similarly, the modified Sperm number is

$$\mathrm{Sp}(R)^4 = \frac{C_D(R)w(R)L^4}{EI} = \frac{C_D^\infty w^\infty L^4}{f(R)g(R)EI} = \frac{\mathrm{Sp}_\infty^4}{f(R)g(R)}. \tag{16}$$

Figure 7(c) shows the *scaled* distance per revolution as a function of the modified sperm number $\mathrm{Sp}(R)$ for all of the data points shown in Fig. 7(b). We see that all the data collapse onto the free space curve, indicating that the two scalings we have introduced appropriately capture much of the dynamics due to the tube. We also emphasize that the evaluation of the coefficients in the expansion of the functions $f(R)$, $g(R)$ used only the simulation data for the *rigid* helical filaments in tubes of varying radii. The collapse of all data, including data from the simulations of the flexible helical filaments, is a good indication that the influence of the tube appears mostly in the form of draglike forces and not as a consequence of deformations of the filaments. However, we see that there is greater variation in the scaled distance per revolution associated with larger Sp, because the changes in shape as a result of the confinement are more pronounced for the more flexible swimmers.

C. Flexible swimmer in tube: Not aligned with tube axis

In the simulations presented above, where the swimmer was initially launched so that its axis coincided with the axis of the tube, the actuated swimmer continued to remain centered. Here we examine how the swimming trajectory would change if the initial position of the helix were not aligned with the tube axis as in Fig. 8. Would the swimmer eventually hit the wall? Would it straighten out its path to swim down the center of the tube? Moreover, how does this depend upon

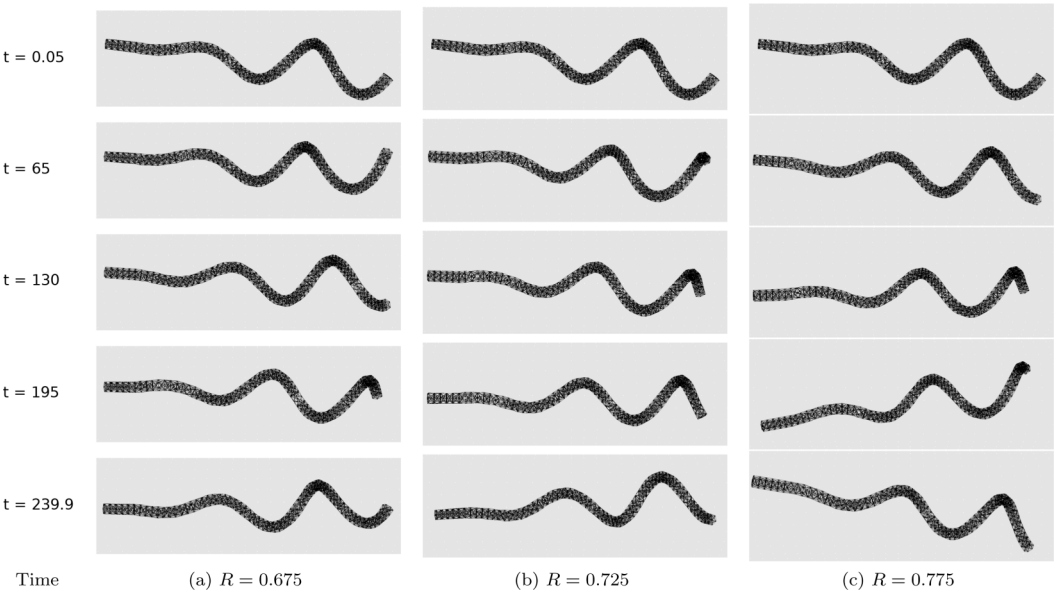

FIG. 9. Side view of the flagellum in three tubes of different radii. Each column shows five snapshots corresponding to a particular tube radius. Each filament was initially angled 0.1 rad away from the central axis of a tube.

the radius of the tube? Here we present three simulations for a flexible swimmer with $k = 300$ driven by a rotlet strength of $\sigma = 5$ inside of tubes of radii $R = 0.675, 0.725, 0.775$.

Figure 9 shows a sequence of snapshots in time of the swimmer in tubes of increasing radii, where the initial orientation of the helical filament formed a nonzero angle with the tube centerlines as in Fig. 8. The forward progression is suppressed in these projected images. In each of the three simulations, we see that the helical shape achieved is basically the same for all three radii. However, we see that in the largest tube $R = 0.75$ [Fig. 9(c)] the angle between the horizontal tube axis and the helix axis has the greatest variation, while this angle in the smallest tube $R = 0.675$ appears to be approaching zero [Fig. 9(a)].

We present another view of the swimming progression in these three simulations in Fig. 10. For each tube radius, there are two columns from the perspective of looking directly down the tube axis. In the right-hand-side column, we see the projection of the helical swimmer coming toward the reader. In the left-hand-side column, we see the projected trajectory of the position of the countertorque, at time zero indicated by a star. Note that if the swimmer were aligned with the tube axis, this projected trajectory would be a single point. Figures 10(d)–10(f) give three-dimensional views of the trajectories of the swimmers, this time looking down the tube as the swimmer moves away from the reader. We see that in the smallest tube ($R = 0.675$), the swimmer exhibits centering behavior, with a helical trajectory whose radius is getting smaller with time. In the largest tube ($R = 0.775$), the swimmer's helical trajectory carries it toward the tube walls, and, in fact, because we are not including repulsion in this model, the simulation is suspended when the swimmer hits the wall. Intriguing behavior is seen in the middle-sized tube ($R = 0.725$), where the swimmer settles upon a limit cycle such that it rolls around the tube in a periodic manner, as can be seen by the projected circular trajectory of the counter-rotlet in Fig. 10(b), and the three-dimensional helical trajectory in Fig. 10(e).

The above examples show that when the initial orientation of the swimmer is perturbed slightly from alignment with the axis of the tube, three classes of swimming trajectories emerge. These classes of swimming trajectories are consistent with the swimming trajectories computed by Shum and Gaffney [29] for bacterial cells swimming between two planar boundaries. For large plate gaps,

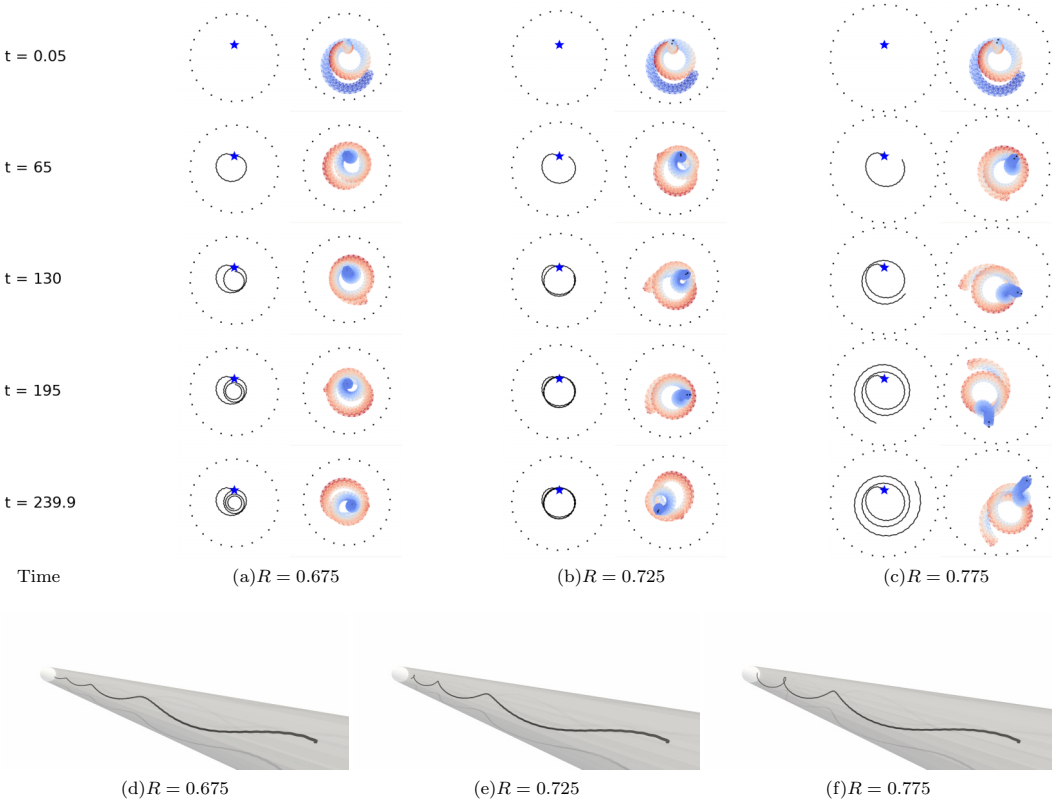

FIG. 10. Axial view of the snapshots in Fig. 9. Each flagellum was initially angled 0.1 rad away from the central axis of a tube. (a) Flagellum and trajectory of the centerpoint of the front cross section for a tube radius of $R = 0.675$. (b) Flagellum and trajectory of the centerpoint of the front cross section for a tube radius of $R = 0.725$. (c) Flagellum and trajectory of the centerpoint of the front cross section for a tube radius of $R = 0.775$. [(d)–(f)] Perspective views of the trajectory of the front point as the flagellum swims down the tube.

cells with sufficiently long helical flagella were attracted to the wall, while for very narrow gaps, the swimmer relaxed to a trajectory midway between the walls. At some intermediate spacing, the swimmer "bounced" repeatedly from wall to wall.

IV. CONCLUSIONS

In summary, we have considered the swimming of a flexible helix both in free space and in a capillary tube. When driven by a fixed torque-countertorque system, the swimming velocity of the helical filament decreases with flexibility but its rotational velocity increases. We find that the swimming performance, when measured by distance traveled per revolution, is well described by the Sperm number. We have also demonstrated that buckling of the filament occurs for the most flexible helices actuated with large rotlet strengths (Sp > 4.7).

For the same flexible helices driven by a fixed torque-countertorque swimming along the centerline of a tube, we find that the swimming speed increases with confinement, as does the distance traveled per revolution. This enhanced swimming performance decreases with helix flexibility. Using a modified Sperm number that accounts for the surface of the tube's effect on drag coefficients, we again find that swimming performance in the tube can be well described by this nondimensional parameter.

When the alignment of the swimmer is perturbed from the tube axis, we find that for larger tubes, the swimmer will eventually hit the boundary of the tube. However, for tubes of smaller diameter, the helical swimmer actually centers itself to align with the tube axis. This finding, along with similar results for swimmers between planar boundaries [29], suggests the provocative idea that bacterial cells may have an easier time breaking through a tightly packed porous medium with small pores. Bacteria moving through large pores are likely to adhere to the matrix.

The model swimmer considered above consists of an elastic helical filament driven by an applied torque and a virtual cell body represented only by an applied countertorque. The drag forces due to a finite-sized cell body are not included. Previous work has shown that the details of cell body shape affect swimming trajectories near planar boundaries [29,30]. We expect that our current model results would be consistent with those of a swimmer propelling a small, spherical cell body. An extension of this model that explicitly represents body shape will examine whether changes in swimming dynamics are observed.

Data are publicly available through the Gulf of Mexico Research Initiative Information and Data Cooperative (GRIIDC) at Ref. [31].

ACKNOWLEDGMENTS

This research was made possible in part by a grant from the Gulf of Mexico Research Initiative and in part by the National Science Foundation Grant No. DMS-1043626. The authors would like to thank Kyriakos Papadopoulos and Mengyuan Zheng for helpful discussions.

[1] E. Lauga, Bacterial hydrodynamics, Annu. Rev. Fluid Mech. **48**, 105 (2016).
[2] N. W. Charon and S. F. Goldstein, Genetics of motility and chemotaxis of a fascinating group of bacteria: The spirochetes, Ann. Rev. Genetics **36**, 47 (2002).
[3] J. T. Pham, A. Morozov, A. J. Crosby, A. Lindner, and O. du Roure, Deformation and shape of flexible, microscale helices in viscous flow, Phys. Rev. E **92**, 011004(R) (2015).
[4] L. Zhang, J. Abbott, L. Dong, K. E. Peyer, B. J. Kratochvil, H. Zhang, C. Bergeles, and B. J. Nelson, Characterizing the swimming properties of artificial bacterial flagella, Nano Lett. **9**, 3663 (2009).
[5] L. Ping, V. Wasnik, and E. Emberly, Bacterial motion in narrow capillaries, FEMS Micro. Ecol. **91**, 1 (2015).
[6] Z. Liu and K. D. Papadopoulos, Unidirectional motility of *Escherichia coli* in restrictive capillaries, Appl. Environ. Mocrob. **61**, 3567 (1995).
[7] M. Binz, A. Lee, C. Edwards, and D. Nicolau, Motility of bacteria in microfluidic structures, Microelec. Engr. **87**, 810 (2010).
[8] L. Zhu, E. Lauga, and L. Brandt, Low-Reynolds-number swimming in a capillary tube, J. Fluid Mech. **726**, 285 (2013).
[9] R. Ledesma-Aguilar and J. Yeomans, Enhanced Motility of a Microswimmer in Rigid and Elastic Confinement, Phys. Rev. Lett. **111**, 138101 (2013).
[10] B. Liu, K. Breuer, and T. Powers, Propulsion by a helical flagellum in a capillary tube, Phys. Fluids **26**, 011701 (2014).
[11] L. Li and S. E. Spagnolie, Swimming and pumping by helical waves in viscous and viscoelastic fluids, Phys. Fluids **27**, 021902 (2015).
[12] A. Acemoglu and S. Yesilyurt, Effects of geometric parameters on swimming of micro organisms with single helical flagellum in circular channels, Biophys. J. **106**, 1537 (2014).
[13] R. Cortez, L. Fauci, and A. Medovikov, The method of regularized stokeslets in three dimensions: Analysis, validation, and application to helical swimming, Phys. Fluids **17**, 031504 (2005).
[14] H. Flores, E. Lobaton, S. Méndez-Diez, S. Tlupova, and R. Cortez, A study of bacterial flagellar bundling, Bull. Math. Biol. **67**, 137 (2005).

[15] R. M. Macnab, Bacterial flagella rotating in bundles: A study in helical geometry, Proc. Natl. Acad. Sci. USA **74**, 221 (1977).
[16] L. Turner, W. S. Ryu, and H. C. Berg, Real-time imaging of fluorescent flagellar filaments, J. Bacteriol. **182**, 2793 (2000).
[17] H. Nguyen and L. Fauci, Hydrodynamics of diatom chains and semiflexible fibres, J. Royal Soc. Interface **11**, 20140314 (2014).
[18] S. Lim and C. S. Peskin, Simulations of the whirling instability by the immersed boundary method, SIAM J. Sci. Comp. **25**, 2066 (2004).
[19] H. C. Fu, T. R. Powers, and C. W. Wolgemuth, Theory of Swimming Filaments in Viscoelastic Media, Phys. Rev. Lett. **99**, 258101 (2007).
[20] A. K. Tornberg and M. Shelley, Simulating the dynamics and interactions of elastic filaments in Stokes flow, J. Comp. Phys. **196**, 8 (2007).
[21] E. Wandersman, N. Quennouz, M. Fermigier, A. Lindner, and O. du Roure, Buckled in translation, Soft Matter **6**, 5715 (2010).
[22] N. C. Darnton and H. C. Berg, Force-extension measurements on bacterial flagella: Triggering polymorphic transformations, Biophys. J. **92**, 2230 (2007).
[23] Y. Takano, K. Yoshida, S. Kudo, M. Nishitoba, and Y. Magariyama, Analysis of small deformation of helical flagellum of swimming Vibrio alginolyticus, JSME Intl. J. **46**, 1241 (2003).
[24] N. Coq, O. du Roure, J. Marthelot, D. Bartolo, and M. Fermigier, Rotational dynamics of a soft filament: Wrapping transition and propulsive forces, Phys. Fluids **20**, 051703 (2008).
[25] M. K. Jawed, N. K. Khouri, F. Da, E. Grinspun, and P. M. Reis, Propulsion and Instability of a Flexible Helical Rod Rotating in a Viscous Fluid, Phys. Rev. Lett. **115**, 168101 (2015).
[26] Y. Park, Y. Kim, W. Ko, and S. Lim, Instabilities of a rotating helical rod in a viscous fluid, Phys. Rev. E **95**, 022410 (2017).
[27] F. Nguyen and M. Graham, Buckling instabilities and complex trajectories in a simple model of uniflagellar bacteria, Biophys. J. **112**, 1010 (2017).
[28] R. M. Wham, O. A. Basaran, and C. H. Byers, Wall effects on flow past solid spheres at finite Reynolds number, Ind. Eng. Chem. Res. **35**, 864 (1996).
[29] H. Shum and E. Gaffney, Hydrodynamic analysis of flagellated bacteria swimming near one and between two no-slip plane boundaries, Phys. Rev. E **91**, 033012 (2015).
[30] H. Shum, E. A. Gaffney, and D. J. Smith, Modelling bacterial behavior close to a no-slip plane boundary: the influence of bacterial geometry, Proc. Royal Soc. London, Ser. A **466**, 1725 (2010).
[31] doi.org/10.7266/n7-d849-2x63, https://data.gulfresearchinitiative.org/data/R5.x286.000:0008